Applied Energy 367 (2024) 123468

Contents lists available at ScienceDirect

Applied Energy

journal homepage: www.elsevier.com/locate/apenergy

Dynamic behavior and energy flow of floating triboelectric nanogenerators

Shuxing Xu [a,b,1], Jiabin Zhang [a,1], Erming Su [a,b,1], Chengyu Li [a,b], Wei Tang [a,b], Guanlin Liu [c,**], Leo N.Y. Cao [a,b,d,*], Zhong Lin Wang [a,b,d,e,*]

[a] Beijing Institute of Nanoenergy and Nanosystems, Chinese Academy of Sciences, Beijing 101400, China
[b] School of Nanoscience and Technology, University of Chinese Academy of Sciences, Beijing 100049, China
[c] Center on Nanoenergy Research, Institute of Science and Technology for Carbon Peak & Neutrality, School of Physical Science & Technology, Guangxi University, Nanning 530004, China
[d] Guangzhou Institute of Blue Energy, Knowledge City, Huangpu District, Guangzhou 510555, China
[e] Georgia Institute of Technology, Atlanta, GA 30332, USA

HIGHLIGHTS

- A novel method is introduced for the six-degree-of-freedom analysis of floating triboelectric nanogenerators (F-TENGs).
- The non-rigid models with control variables are universal and close to the real situation.
- F-TENGs' comprehensive attitude tracking and analysis of dynamics/energy under wave excitation are provided.
- The resulting rules can facilitate and guide the structural optimization of F-TENGs for wave-energy conversion.
- Fluid dynamics analysis software is employed to elucidate the rules governing F-TENG parameters.

GRAPHICAL ABSTRACT

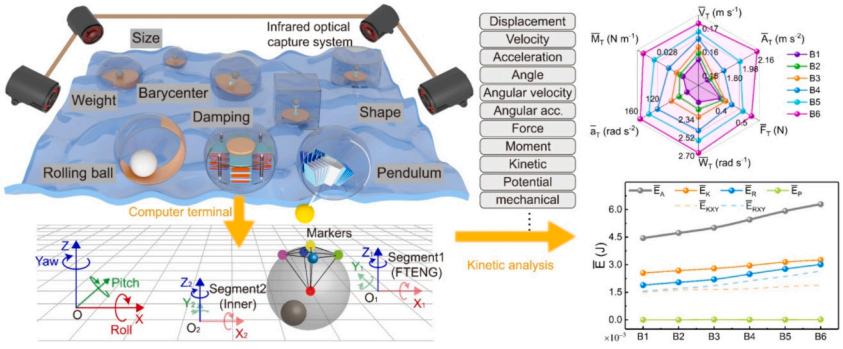

ARTICLE INFO

Keywords:
Blue energy
Triboelectric nanogenerator
Six degrees of freedom test
Kinetics analysis
Optical motion capture system

ABSTRACT

The comprehension of the dynamic behavior and energy flow characteristics of triboelectric nanogenerators on water is a prerequisite for enhancing wave energy conversion efficiency and output performance, yet these data have always been lacking, impeding their progress in harnessing blue energy. Herein, a series of meticulously conducted experiments aim to unveil the interaction between water waves and the geometrical structures of floating triboelectric nanogenerators (F-TENGs). The six degrees of freedom (6DoF) information of various F-TENGs under wave excitation is received for the first time by employing the new high-tech Infrared Optical Capture System and precision numeric analysis. Based on statistical data from 118 research papers, the most universally applicable modes/parameters are systematically explored, as well as the non-rigid body models. The six-dimensional kinematic radar matrices and energy gradient curves, peeled from the calculation and statistics of the 6DoF data, have comprehensively illuminated the dynamic behavior and energy flow of F-TENGs while

* Corresponding authors at: Beijing Institute of Nanoenergy and Nanosystems, Chinese Academy of Sciences, Beijing 101400, China.
** Corresponding author.
E-mail addresses: guanlinliu@gxu.edu.cn (G. Liu), caonanying@binn.cas.cn (L.N.Y. Cao), zhong.wang@mse.gatech.edu (Z.L. Wang).
[1] These authors contributed equally.

https://doi.org/10.1016/j.apenergy.2024.123468
Received 24 December 2023; Received in revised form 7 April 2024; Accepted 11 May 2024

interacting with water waves. These results can serve as an enlightening framework for structural design and facilitate the optimization of F-TENG in harnessing blue energy.

1. Introduction

The vast and ubiquitous ocean waves represent a bountiful source of clean energy, perennially captivating research endeavors within the realm of new energy harvesting [1,2]. Among these pursuits, the Floating Triboelectric Nanogenerators (F-TENGs) [3], which harness energy through frictional and electrostatic induction processes [4–7], have garnered significant acclaim, owing to their high degree of coupling with the operational cycles of sea breeze and ocean waves [8], lightweight construction facilitating effortless buoyancy [9,10], low manufacturing costs [10,11], and scalability for large-scale deployment [1,8]. Consequently, F-TENGs find versatile utility in mechanical wave energy harvesting [12], wireless ocean conditions monitoring [13], water quality assessment [14], and self-powered offshore equipment driving [15]. Based on current output measurements, it is estimated that a three-dimensional network structure of F-TENGs, with a spacing of 10 cm, a depth of 10 m, and excited two to three times per second, covering one square kilometer of the sea surface, can generate 1.15 MW of electrical energy [8,12], effectively meeting the electricity demands of 12,123 residents and thereby significantly mitigating the ever-increasing energy requirements. Although continuous research is dedicated to enhancing the output performance of F-TENG through structural optimization [16,17], novel material synthesis [18], and power management [14,19], several challenges persist, including the impractical coupling methods between waves and F-TENG, a deficiency in systematic dynamic detection and analysis methods, and a tendency toward immoderate parameter optimization [19,20]. Additionally, some F-TENGs are affixed to large floats to raise the waterline and barycenter for improved responsiveness to water waves, resulting in the wasteful utilization of fleeting blue energy and emphasizing the urgency for dynamic research and parameter optimization [21–23]. Hence, conducting dynamic investigations of F-TENGs in response to structural parameter changes under water wave excitation becomes exceptionally crucial.

The dynamical study of F-TENGs is inherently pervasive, as researchers routinely assess their output performance under varying wave intensities and frequencies to observe regular output variations [24,25]. On the other hand, the dynamical study of F-TENGs has been behaved one-sided, lacking comprehensiveness. Previous research has primarily focused on the output, simulation, or dynamic calculations of a specific F-TENG [19,21], with no systematic investigation into the dynamical variations of different or universal F-TENGs. Therefore, understanding diverse F-TENG variations responsive to wave excitations, especially the universal parameters, is crucial for designing structures that can subsequently demonstrate increased sensitivity and enhanced efficiency in converting oceanic energy. There have been prior attempts [26,27] to record the motion of F-TENG within ocean waves by embedding inertial measurement units and examining the kinematic changes resulting from variations in structural parameters [28]. However, this testing method has been limited in its capacity to record the magnitude of acceleration along a single axis unilaterally. Consequently, it fails to track the multidimensional motion characteristics, impeding a comprehensive analysis of the dynamic patterns arising from structural parameter changes under wave excitation. The approaches involving the installation of bulky sensors either inside or on the surface of F-TENGs often tend to interfere with their authentic motion within ocean waves, introducing errors in the test results. Furthermore, under non-uniform and multifield compound interactions, the dynamical patterns obtained from specific F-TENG's variations may not necessarily be applicable to all devices designed for wave energy harvesting. Thus, it is evident that the patterns, deriving from systematically cataloging and analyzing existing F-TENGs, extracting and summarizing conventional parameters and modes in these designs, and conducting standard testing and dynamical calculations, have the potential to serve as universal principles governing the integration of F-TENGs within structures, and play a guiding role in structural optimization and optimal design.

In this work, we systematically reviewed and summarized over 100 papers on F-TENGs published in the past decade, extracting the most prevalent core parameters including the barycenter, weight, diameter, dimensions, essential modes including the roller mode, elastic mode, and assist mode, and fabricated floats under controlled variable conditions. Simultaneously, we established a new Infrared Optical Capture System (IOCS) to record minute markers affixed to the float, thereby capturing its six degrees of freedom (6DoF, including translational motion on the X, Y, Z axes and rotational motion along the X, Y, Z axes, like the coordinate system in Fig. 1a) motion in standard waves. We analyzed dynamic data for F-TENGs, like its velocity, acceleration, forces, angular velocity, angular acceleration, and moments, presented them in radar charts; while the values such as rotational kinetic energy, translational kinetic energy, gravitational potential energy, and total mechanical energy were depicted in curve plots; and conducted simulations using ANSYS AQWA software, together to analyze F-TENGs' response under wave excitation. Standardized testing and modeling of these universal modes and essential parameters can effectively assist in the future structural design and optimization of F-TENGs. Additionally, this visually integrated testing approach offers an effective method for F-TENG trajectory tracking, multidimensional analysis, networked validation, and simulation model verification.

2. Experimental section

2.1. Test environment

The IOCS system used for testing was constructed with the assistance of NOKOV Corporation, utilizing their NOKOV Motion Capture System, which comprises four high-definition cameras, a splitter, a three-axis gimbal, markers, and other components. Among these components, the lenses play a central role in the entire IOCS system, as their resolution and field of view determine the effectiveness and precision of F-TENG motion tracking. The optical lenses are equipped with illuminating LED lights that emit specific wavelengths of infrared light onto the markers, which are points located on the rigid bodies. Due to the reflective properties of the material on the marker points' surface, they reflect the infrared light back into the lenses, and then processed through image capture and algorithmic analysis, allowing us to obtain the two-dimensional coordinates of the marker points within the lens. After lens calibration, the two-dimensional coordinates obtained from multiple lenses can be used to calculate the three-dimensional coordinates of the marker points. Through testing, it was determined that the optimal capture state for the marker points was achieved when their size was 8 mm, and the stability was highest when there were >4 markers. In this setup, the positioning accuracy reached the submillimeter level (0.2 mm, as shown in Table S1), with precision in acceleration and angular velocity reaching 0.0016 m/s^2 and 0.0012 rad/s, respectively. The wave generation environment was set up with the assistance of engineers, and it included a wave tank with dimensions of $1.2 \times 1.0 \times 1.0$ m, equipped with a Jiebao RW20 wave generator with a power rating of 50 W. Except for cases where the influence of external stimuli needs to be tested, all other tests utilize resonant waves generated by a wave-making pump installed horizontally, with a strength of 15 cm and a frequency of 1.1 Hz.

2.2. Production of rigid floats

The framework of the floats was obtained through 3D printing using transparent photosensitive resin to ensure material transparency. The structural design software employed was 3Dmax, which allowed for the direct calculation of volume from the exported STL format, and multiplying the volume by the material density yielded the weight of the outer shell. The counterweights were fabricated from brass blocks (with an approximate density of 8.5 g/cm^3) using machining processes, with their dimensions and thickness adjusted through calculations to achieve the desired mass for each counterweight block. The detailed structures of the barycenter, weight, size, and shape are shown in Supporting Information, with the exception of the barycenter variation experiment, all other floats maintain their barycenter at approximately one-third along the diameter/height; exception of the weight variation, the total weight of the floats remains consistent across experiments; and apart from the shape variation experiment, all floats use a 12 cm smooth spherical shell. All floats consist of two halves, then bonded together using waterproof glue after filling with the corresponding ballast and markers.

2.3. Production of float in roller, elastomer, and assist mode

The manufacturing and assembly process of non-rigid, damping-type floats is the same as mentioned above, with the weight and container's barycenter controlled to be located at one-third of the diameter. The only difference is the disc-shaped counterweight has been replaced with a circular ring-shaped one. In the roller mode, the weights of the wooden, plastic, ceramic, and iron balls are 7.77, 11.06, 30.19, and 64 g, respectively. When investigating the motion of the internal roller, identical diameter marker points were used as the rolling ball. In elastomer mode, four lightweight acrylic columns were employed to constrain the spring's path, with a thin acrylic plate supporting the weight, and marker points affixed to the moving block. Then, the damping components were adhered beneath the shell, and the block's position was approximately at the overall barycenter of the float. When investigating the stiffness coefficient, different springs with various wire

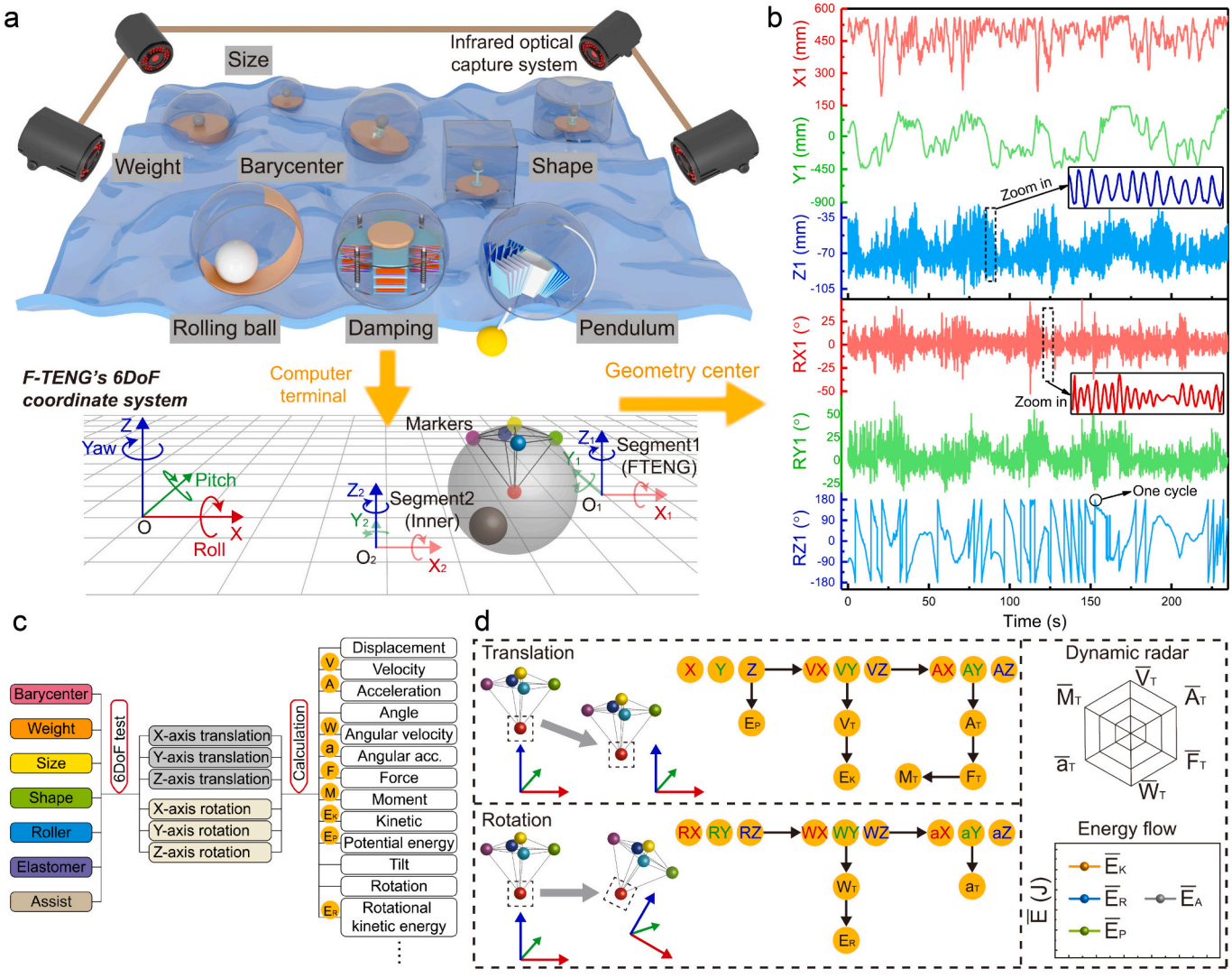

Fig. 1. Test setup and dynamics analysis. (a) Schematic diagram of the IOCS system testing the motion of different F-TENG floats in resonant waves. The IOCS uses the principle of infrared reflection/refraction to capture the markers attached to the F-TENG and record their positions. The computer terminal would decode the 6DoF (three-axis translation, X, Y, Z and three-axis rotation, Roll, Pitch, Yaw) information of the marker composed segment (which can be multiple). (b) 6DoF at the geometric center of F-TENG float output by IOCS under wave excitation. (c) Overall flow chart of dynamics calculation. (d) The tested floats can yield a multitude of characteristic information in translation, rotation, and energy through dynamic calculations, including differentiation, vector synthesis, and parameters substitution, and statistics for 6DoF. After three rounds of testing (100,000 frames at 16.67-min wave excitation), the $\overline{V}_T$, $\overline{A}_T$, $\overline{F}_T$, $\overline{W}_T$, $\overline{a}_T$, and $\overline{M}_T$ are presented in radar charts, while the $\overline{E}_K$, $\overline{E}_R$, $\overline{E}_P$, and $\overline{E}_A$ are depicted in curve graphs, allowing for a comprehensive analysis of F-TENG performance in wave conditions.

diameters (0.1, 0.2, 0.3, 0.4 mm) were substituted, and when exploring different weights, the thickness of the counterweights was varied (30, 60, 90 g). In the assist mode, the pendulum rod was also created through 3D printing and adhered to the main body using waterproof glue. The pendulum rod length was varied in increments of 0, 2, 4, 6 cm, and the pendulum was selected from four materials (wood, plastic, ceramic, and steel) with weights of 23.47, 44.25, 71.48, and 268 g, respectively.

2.4. Float test and kinetic calculations

The waves used for testing were harmonic waves, where the intensity and frequency of the waves remained relatively constant over time. To ensure the accuracy, each sample calculation involved capturing 100,000 frames, which corresponds to the float's motion over 16.67 min (camera operating frequency is 100 Hz). After initial processing, 100,000 sets of 6DoF information were obtained from the samples. Subsequently, these data were differentiated over time to derive V, A, W, and a. After vector synthesis, V_T, A_T, W_T, and a_T were obtained, and these values were multiplied by the corresponding coefficients to calculate F_T, M_T. Finally, the $\overline{V}_T$, $\overline{A}_T$, $\overline{F}_T$, $\overline{W}_T$, $\overline{a}_T$, and $\overline{M}_T$ were computed by taking the mean of these calculations across the 100,000 samples. The energy calculations involve substituting these values into the formulas to determine the $\overline{E}_K$, $\overline{E}_R$, $\overline{E}_P$ of the float, which are then summed to obtain $\overline{E}_A$. The averages calculated from three rounds of testing are presented on the kinematic radar chart and energy curve chart. Data decoding for the marker points is performed using NOKOV's specialized software Suixing and subsequent kinematic calculations are carried out in collaboration between Matlab and Origin.

2.5. Simulation settings

Dynamic simulations of floats are all conducted in the ANSYS AQWA environment. First, the model, which matches the actual testing size, is designed using SolidWorks modeling software. Subsequently, it is imported into the ANSYS AQWA software, and the analysis is conducted by utilizing the Hydrodynamic Diffraction module. The dynamics analysis in ANSYS AQWA can be simplified into the following steps: model import, model parameter configuration, meshing, setting wave conditions and spectra, and conducting result calculations. In those processes, the dimensions and shape of the float can be adjusted using modeling software, while parameters like the barycenter and draft can be fine-tuned within ANSYS AQWA to match the actual waterline depth, as shown in Table S2. Additionally, in the result calculation phase, the pressure distribution and changes on the float in motion amplitude are determined by adding the Hydrostatic, Pressure-Motions modules. Furthermore, the Solution section of the Hydrodynamic Diffraction module can be linked to the Hydrodynamic Response module for time-domain and frequency-domain analysis of the floater. However, given that the focus of this experiment is not on these aspects, no further research was conducted in this area.

3. Results

3.1. Test setup and dynamics analysis

The constructed IOCS (Figs. 1a and S1) employs four active high-speed cameras (Table S1) to record the two-dimensional coordinates of tiny markers (diameter 8 mm) using the principles of infrared light reflection [29]. Through computations in the upper-level software, these two-dimensional coordinates are transformed into their corresponding three-dimensional positions and kinematic data (Movie S1). Following a comprehensive review of prior research, we have identified seven essential parameters/modes: barycenter, weight, size, shape, roller, elastomer, and assist (pendulum), and produced floats with predetermined geometric attributes using a controlled-variable methodology. Subsequently, we affixed multiple markers ($n > 4$) to the surface, center, and internal moving components of the float, transforming these points into rigid segments, and employed the IOCS to simultaneously measure the kinematic information of these rigid bodies' 6DoF. To simulate real, sufficiently high-energy ocean waves, a wave generation system (Fig. S2) was constructed, which within a large-capacity wave pool (1.2 × 1.0 × 1.0 m, the water depth is 0.6 m, Fig. S1), with ten high-power wave pumps (50 W) operating simultaneously at the same frequency and power to produce continuous and resonant standard waves to investigate the dynamic principles governing float models, example 6DoF at the geometric center of the float shown in Figs. 1b and S3 (translation in X1, Y1, Z1 and rotation in RX1, RY1, RZ1).

Then, we conducted dynamic calculations (Figs. 1c and S4) using the 6DoF information obtained from the long-term testing (100,000 frames, approximately 16.66 min). In translation, three-axial velocity is obtained by differentiating the displacements along those axes, and then differentiation yielded accelerations. After vector summation and averaging, the total average velocity ($\overline{V}_T$) and total average acceleration ($\overline{A}_T$) are obtained (Fig. S5), and the total average force ($\overline{F}_T$) and total average torque ($\overline{M}_T$) are obtained by multiplying the own mass and moment arm respectively. In the realm of rotational motion, we obtained the angular velocities along each axis by differentiating the rotation angles (Fig. S6), further differentiating to determine the angular accelerations, and subsequently averaging and vector-summing to derive the total average angular velocity ($\overline{W}_T$) and total average angular acceleration ($\overline{a}_T$). Following dynamic calculations (formulas 1, 2, 3 and 4), the 6DoF information can yield a multitude of additional data, including kinetic energy ($\overline{E}_K$), rotational kinetic energy ($\overline{E}_R$), potential energy ($\overline{E}_P$), and total mechanical energy ($\overline{E}_A$), as depicted in Fig. 1d. In the subsequent analysis, the information encompassing $\overline{V}_T$, $\overline{A}_T$, $\overline{F}_T$, $\overline{W}_T$, $\overline{a}_T$, and $\overline{M}_T$ is subjected to multiple averaging processes ($n = 3$) and presented in a radar chart, while $\overline{E}_K$, $\overline{E}_R$, $\overline{E}_P$, and $\overline{E}_A$ (same averaged three times) are displayed in a curve chart, which two graphical representations serve to illustrate the patterns of variation in F-TENG parameters and structural changes.

$$\overline{E}_K = \frac{1}{2} M \overline{V}_T^{\,2} \tag{1}$$

$$\overline{E}_R = \frac{1}{2} I \overline{W}_T^{\,2} \tag{2}$$

$$\overline{E}_P = M\, G\, \overline{\Delta Z} \tag{3}$$

$$\overline{E}_A = \overline{E}_P + \overline{E}_K + \overline{E}_R \tag{4}$$

in which, M and I respectively represent the mass and moment of inertia of the float (the detailed calculation process refers to Note 1), $G = 9.80$ m/s^2 stands for the gravitational acceleration of Beijing, and $\overline{\Delta Z}$ represents the average vertical displacement change.

3.2. Geometric parameter variations in F-TENG

In the investigation of the variations in geometric parameters of the F-TENG rigid model, we employed stereo lithography appearance 3D printing using transparent photosensitive resin to fabricate both the outer shell and internal support of the float (Fig. S7), which allowed us to precisely control the variables of the barycenter, weight, dimensions, and shape. When exploring variations in the barycenter, a spherical float with a 12 cm diameter was utilized to gradually move the internal counterweight upward to obtain the hierarchically rising barycenter, as shown in Figs. 2a(i) and S8. Subsequently, following constant wave testing and corresponding calculations, dynamic radar chart and energy curve graph were obtained to showcase the kinetic and energy variations resulting from the incremental rise in the F-TENG barycenter. From

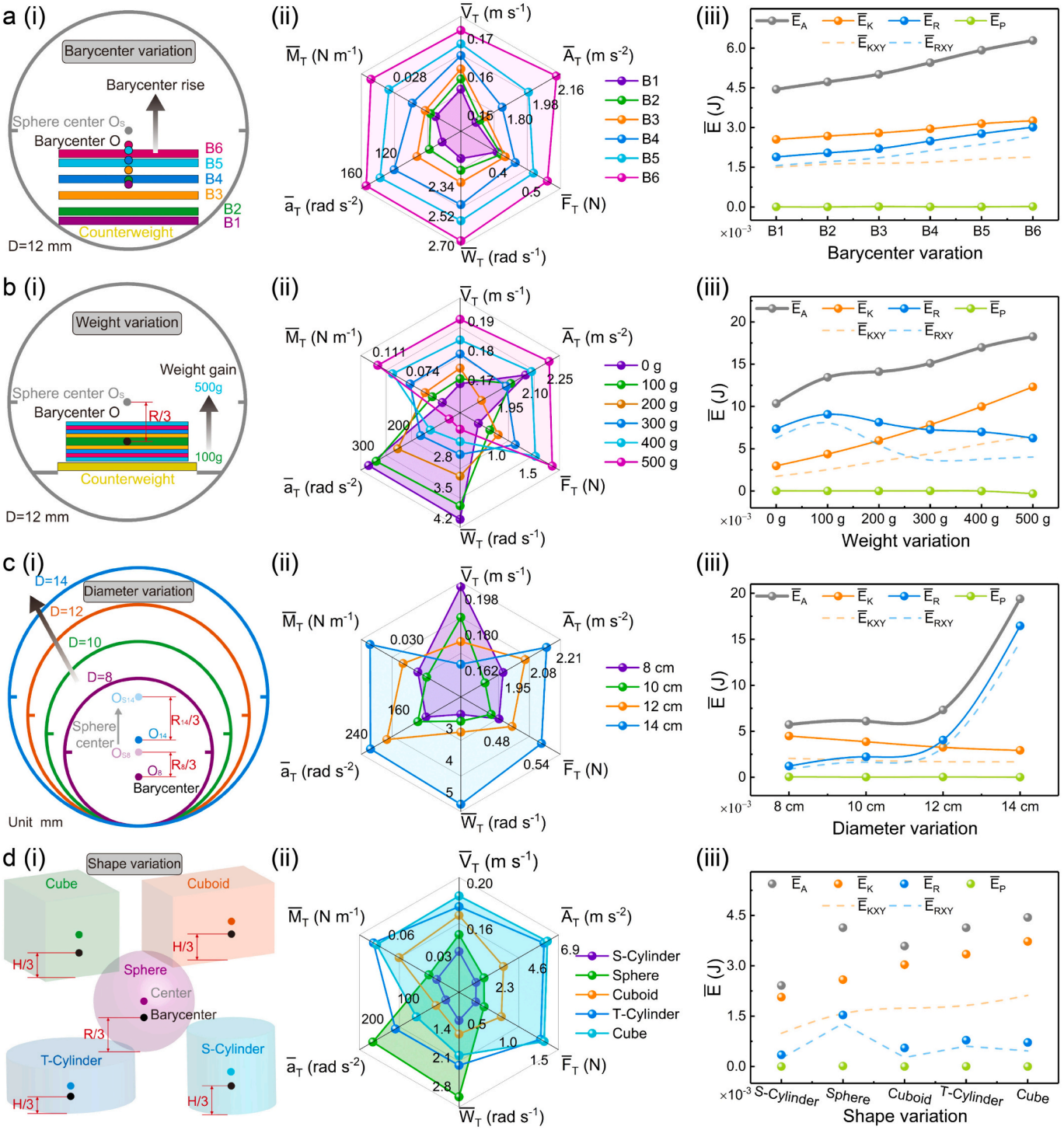

Fig. 2. Geometric parameters variation in F-TENG. The (i) schematic diagrams, (ii) dynamic radar charts, and (iii) energy curve graphs illustrating the principles under variations in (a) barycenter, (b) weight, (c) dimensions, and (d) shape. The displayed data represents the average values obtained after three independent trials.

the radar chart, it becomes evident that the six-dimensional dynamic data of F-TENG (Fig. 2a(ii)) progressively increase as the barycenter rises. Analyzing from an energy perspective (Fig. 2a(iii)), as the barycenter rises, the float's oscillation intensifies, resulting in a significant boost in rotational kinetic energy and, consequently, an overall increase in mechanical energy. This suggests that gradually elevating the F-TENG's barycenter proves advantageous for harvesting mechanical energy in the direction of oscillation [30,31].

In investigating variations in weight or draft, the barycenter of the 12 cm spherical float was kept constant (at one-third along the diameter), while additional counterweights were incrementally added at the barycenter from 100 to 500 g, as illustrated in Figs. 2b(i) and S9. From the radar chart and energy curve graph, it is apparent that F-TENG with higher weight exhibits superior translational performance, as evidenced by higher $\overline{V}_T$, $\overline{A}_T$, $\overline{F}_T$ and $\overline{E}_K$, conversely, with rotational performance obviously decrease (Figs. 2b(ii) and (iii)), even at maximum draft almost drops to zero. Which implies that, when collecting rotational wave

energy, opting for heavier configurations is less favorable [25].

In investigating size variations, we increased the spherical diameter while simultaneously controlling the overall weight and barycenter of the float by using machine cutting and adjusting the positions of counterweight, which allowed us to create floats of 8, 10, 12, and 14 cm in diameter, as depicted in Figs. 2c(i) and S10. Through testing and calculations, it was observed that an increase in size would diminishes the translational performance of the F-TENG, resulting in a decrease in $\overline{E}_K$ and $\overline{V}_T$ (Fig. 2c(ii)). However, under the same wave excitation, and with constant weight and barycenter conditions, this increase in size intensifies the rotational motion of the float, leading to a notably enhanced improvement in rotational performance [21], even by several times (Fig. 2c(iii)).

Following that, we adhered to the principle of equal volume with 12 cm spherical float and designed rectangular, cuboid, short cylindrical, and tall cylindrical floats [28,32] while keeping the weight constant and the barycenter positioned at one-third along the height, as shown in Figs. 2d(i) and S11. After conducting tests, it was observed that spherical and short cylindrical floats exhibit minimal translational performance but possess substantial rotational kinetic energy, particularly the spherical float with the lowest moment of inertia (Figs. 2d(ii) and (iii)). Floats with flat and angular surfaces, such as cube and cuboid shapes,

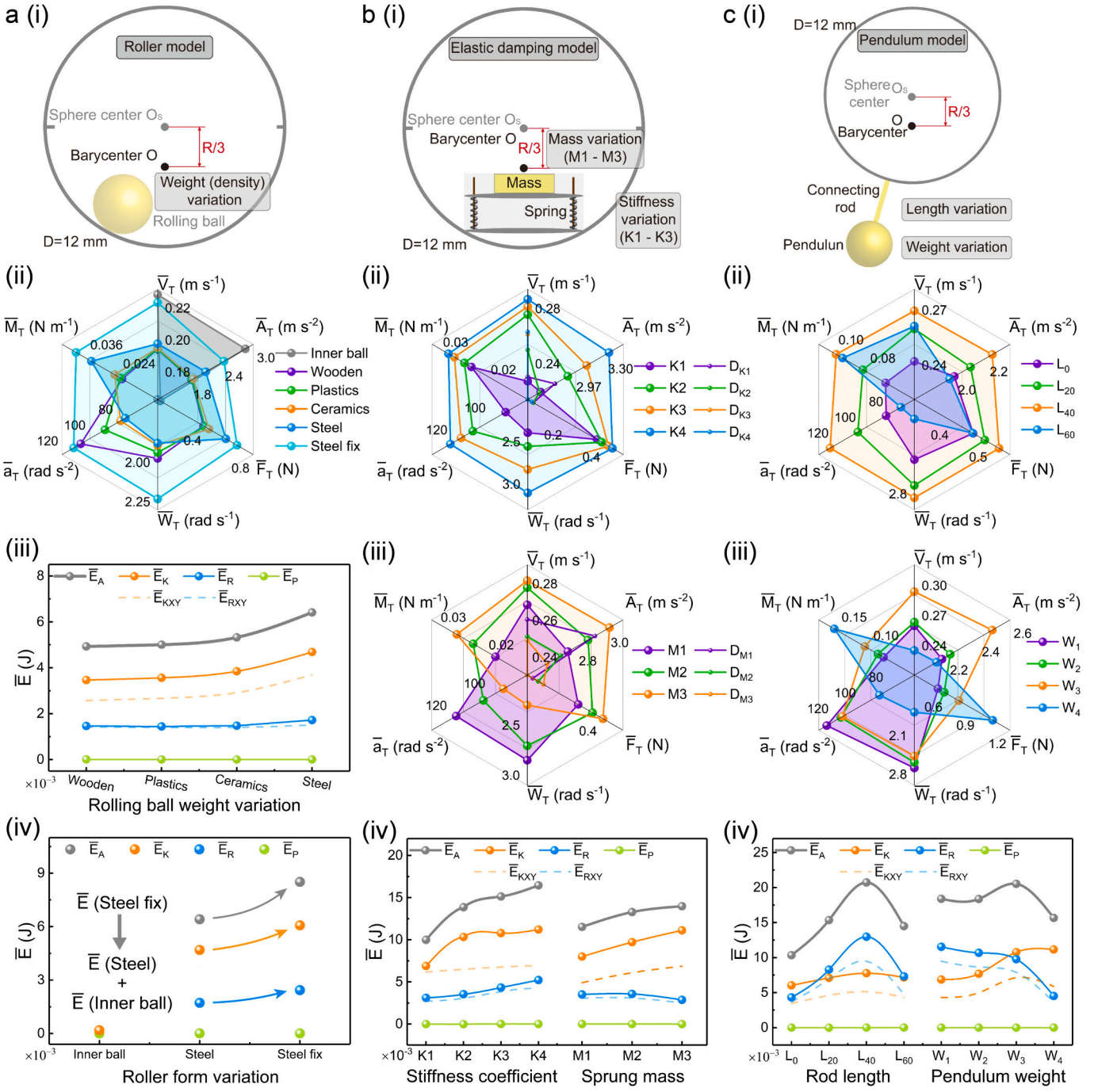

Fig. 3. Roller, elastomer, and assist models in F-TENG. The (i) schematic diagrams, (ii or iii) dynamic radar charts, and (iii or vi) energy curve graphs illustrating the principles after changes in the (a) roller mode, the stiffness coefficient and support weight in the (b) elastomer mode, and the rod length and pendulum weight in the (c) assist mode. Among them, "Inner ball", "D_{K1}-D_{K4}", and "D_{M1}-D_{M3}" in Figures a(ii), and b(ii), (iii) represent internal rolling ball, internal spring stiffness coefficient, and elastic damping weight respectively. The displayed data has also undergone averaging after three independent trials.

exhibited significant translational performance when subjected to water wave impacts, but slightly lagged in rotational motion due to their higher moment of inertia. Therefore, when selecting the F-TENG shape, it is possible to consider similar types of shapes based on the dynamic radar chart and energy change curve to meet specific requirements, such as peak power density, sensitivity, and omnidirectional collection [33].

3.3. Roller, elastomer, and assist modes in F-TENG

The floats tested in Fig. 2 were all rigid, assuming no relative movement and no damping inside. However, real F-TENG devices are non-rigid and involve damping, generating charge transfer through internal relative motion [24,25]. Therefore, after summarizing previous work, we derived three universally modes—roller [26,30], elastomer [22,25], and assist [19,34,35]—that cover all structural designs and align more closely with the practical F-TENG scenario. Within a 12 cm spherical shell, a defined weight and a one-third position barycenter were set, and corresponding damping units were added. Under consistent and resonant wave testing, the output of 100,000 frames of images from IOCS was statistically analyzed as a sample. In the roller model, we investigated three scenarios: the roller's weight, motion, and influence. In exploring the rollers' weight, we progressively altered inner balls of the same diameter and different materials (e.g. wood, plastic, ceramic, steel), the weight of the roller is gradually changed from 7.7 to 64 g (Figs. 3a(i) and S12). With the increment in roller weight, the translational performance of the float, including parameters like $\overline{V}_T$, $\overline{A}_T$, $\overline{F}_T$, and $\overline{E}_K$, markedly increased (Fig. 3a(ii)). However, the rotational performance, as indicated by $\overline{W}_T$ and $\overline{a}_T$, decreased, resembling the patterns observed with changes in weight for rigid floats. Then the $\overline{E}_R$ leveled off slightly in the energy graph when accounting for the moment of inertia (Fig. 3a(iii)). In exploring the rollers' motion, the internal roller exhibits $\overline{V}_T$ and $\overline{A}_T$ several times greater than those of the float itself (as the gray matrix in Fig. 3a(iii)), indicating that the internal rollers frequency response is significantly higher than that of the wave and F-TENG shell itself, resulting in multiple back-and-forth movements within a single wave excitation. In exploring the rollers' influence by fixing the internal roller and investigating the impact of inertial damping on F-TENG (as shown in Fig. 3a(iv) with steel and steel fix), we observed increase in distinctive dynamic quantities and energy, indicating that the internal roller diminishes F-TENG's motion performance in wave.

Next, we investigated the impact of transitioning from fully free movement represented by the roller) to partially constrained internal components (like springs and elastic supports) on the dynamics of F-TENG. This entailed investigating the impact of internal spring stiffness (K1-K4, the wire diameter changes from 0.1 to 0.4 mm) and weight (M1-M3 in the range of 30 to 90 g) on the motion performance of F-TENG by replacing internal springs and adding internal counterweights, as illustrated in Figs. 3b(i) and S13, while also documenting the motion trajectories of internal springs under stress waves. As the spring stiffness coefficient continuously increased, the float gradually transitioned from non-rigid with damping to rigid, exhibiting the same dynamic patterns as when the rolling ball was fixed in the six-dimensional radar chart, as well as energy changes (Figs. 3b(ii) and (vi)). When increase the weight of spring support likewise exhibited the same patterns as rigid-weighted floats, with an increase in translational performance and a marked decrease in rotational performance (Figs. 3b(iii) and (vi)). The internal spring block (D_{K1}-D_{K4} in Fig. 3b(iii), D_{M1}-D_{M3} in Fig. 3b(iii), and zoom-in graph in Fig. S14) illustrating that an increase in spring stiffness results in reduced $\overline{A}_T$ and higher $\overline{V}_T$ of the internal damping, while adding weight leads to both decreased. In general, augmenting stiffness and weight will transition non-rigid to rigid type, which is not conducive to the movement of the internal inertial object.

In addition to the most common roller and elastomer modes, another common approach is the assist mode, which involves increasing the output of F-TENG through external gears [36], internal/external pendulums [19,35,37], and biomimetic structures [38]. Here, we have selected the most common and fundamental pendulum type to investigate the dynamic changes in F-TENG after the application of assistance. By systematically changing variables, we explored the influence of rod length (L1-L4, from 0 to 6 cm), pendulum weight (W1-W4, from 23.47 to 268 g), and pendulum dimensions (W1-W4, from 3 to 6 cm) on the dynamic performance of the F-TENG dynamism (Figs. 3c(i), S15, and S16). As the pendulum rod length increases, the dynamic performance of the float exhibits a trend of initial enhancement followed by a decrease, primarily reflected in the area of the radar matrix and energy curve (Figs. 3c(ii) and (iv)). Notably, the application of appropriate assistance, such as L_{40}, shows a significant promotional effect compared to the absence of assistance, as seen in L_0. When the pendulum weight increases (size variation shown in Fig. S17), similarly to the trend observed in weight variations, it leads to improvements in translational performance (Fig. 3c(iii) $\overline{V}_T$, $\overline{A}_T$, and $\overline{F}_T$, and Fig. 3c(iv) $\overline{E}_K$), accompanied by a decrease in rotational kinetic energy (Fig. 3c(iii) $\overline{W}_T$ and $\overline{a}_T$, and Fig. 3c(iv) $\overline{E}_R$). In summary, it is evident that appropriately increasing the arm length (rod length) and applied force (pendulum weight) at the assist mode can effectively enhance the absorption of mechanical energy by F-TENG.

3.4. Response of the same F-TENG to different wave excitations

To explore the response of F-TENG under varying external wave excitations and its associated alterations in 6DoF, energy, and electrical output (Fig. S18), a spherical floater with a barycenter at B3, no added weights, and a diameter of 12 cm was designed and tested under waves generated at different heights, frequencies, and modes by altering the operation of the wave-making pump. When the F-TENG is placed in waves where the frequency and mode remain constant but the height continuously increases (5, 10, 15, 20 cm, Fig. 4a(i)), all values in the dynamics radar matrix and energy curve gradually increase, as shown in Figs. 4a(ii) and (ii). As the wave frequency increases, inevitably enhancing the intensity of wave resonance, it also leads to the increment in the dynamics and energy (Fig. 4b) of F-TENG. With the wave-making pumps operating at the same output power and frequency, placing them horizontally and vertically (Fig. 4c(i)) respectively generates waves of different forms. Following testing, it was observed that waves generated in the vertical orientation yield significantly higher levels of kinetic energy (Fig. 4c(ii)), manifesting notably in $\overline{E}_P$, $\overline{E}_R$, and $\overline{E}_A$, but may be constrained in $\overline{E}_K$ and $\overline{E}_{KXY}$ (Fig. 4c(iii)).

3.5. Comparison and simulation analysis of variations

To further analyze the patterns of F-TENG response to wave excitation following structural changes, we conducted a cross-comparison among various parameters and modes (Fig. 5a). Select a reference float with a similar structure, such as "B4", "0 g", "12 cm", "spherical", to facilitate the analysis of patterns following parameter changes (Figs. 5b(i) and (ii)). The intuitive change resulting from the upward barycenter is an increase in all six-dimensional dynamic matrices, indicating a more pronounced stress response in F-TENG and easier changes in posture. The obvious positive impact of weight is manifested in the applied force and torque, attributed to the large weight coefficient, while its negative influence is a reduction in rotational performance, resulting in smaller tilt angles and rotational capabilities. Increasing the size results in a larger contact area with water waves (Fig. 5a), making the 14 cm spherical floater exhibit optimal rotational performance. Floater shapes with flat surfaces and edges are more susceptible to the impact force of water waves, resulting in higher $\overline{V}_T$, $\overline{A}_T$, and $\overline{F}_T$. However, their lack of smoothness makes them less agile in terms of rotation, leading to poorer rotational performance. To further substantiate the aforementioned results, we employed the professional dynamics analysis software ANSYS AQWA (Table S2) to simulate real

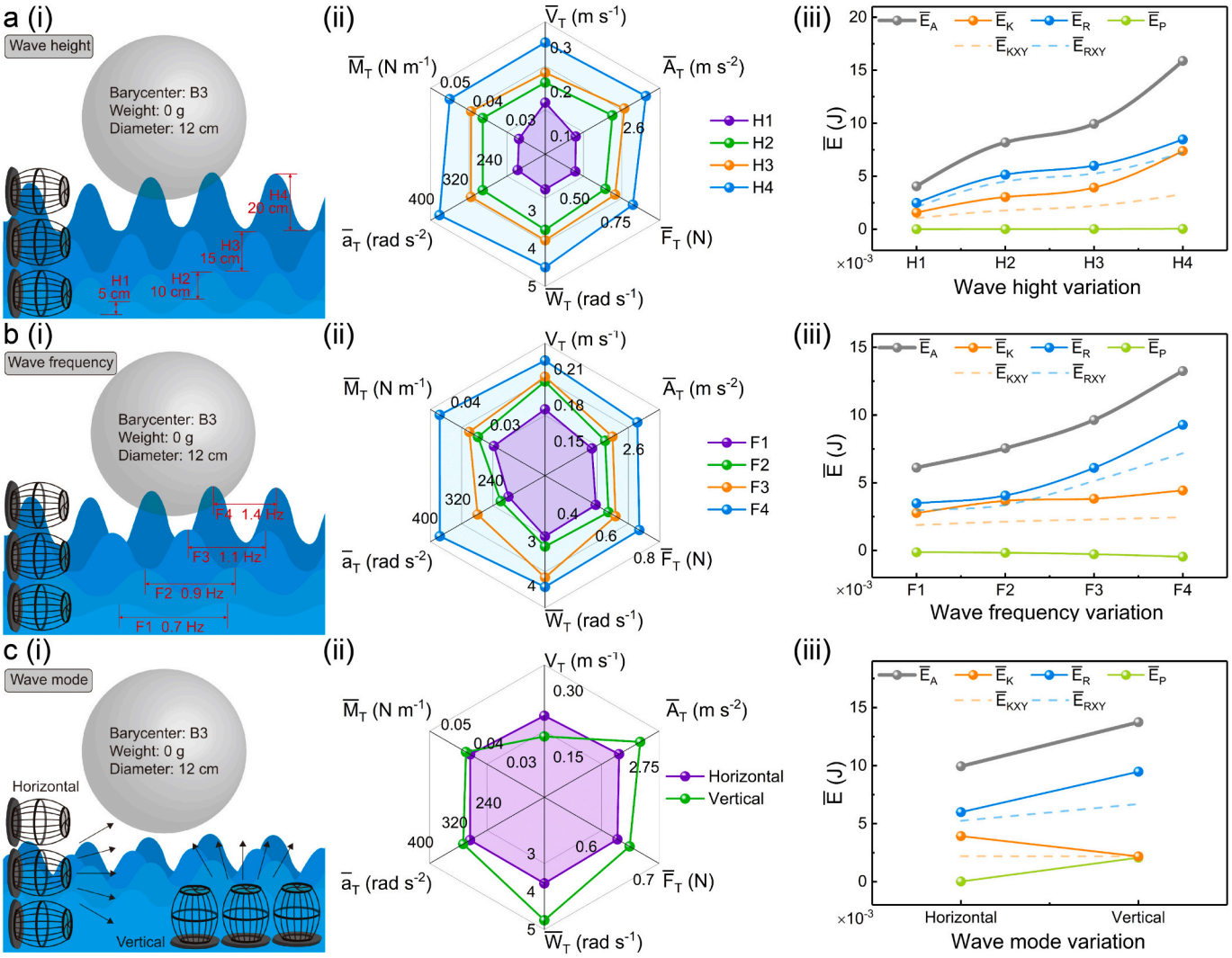

Fig. 4. Response of the same F-TENG to different wave excitations. The (i) schematic diagrams, (ii) dynamic radar charts, and (iii) energy curve graphs of the same F-TENG under different (a) wave heights, (b) wave frequencies, and (c) wave generation methods (wave pumps in horizontal and vertical directions). The data presented reflects the average values obtained from three separate trial experiments.

testing scenarios (with a wave height of 100 mm and frequency of 1 Hz). By modifying model size and material properties (such as Young's modulus and moment of inertia) to change the barycenter, weight, dimensions, and shape of the float (Fig. 5c), we obtained results reflecting the forces acting on the floater, including variations in surface pressure distribution (unit mN), through simulations in the Hydrodynamic Diffraction module. Comparing the simulation results, it was observed that as the floater's barycenter rises (Fig. 5c(i)), draft increases (Fig. 5c (ii)), dimensions enlarge (Fig. 5c(iii)), or when transitioning from a spherical to a cuboidal shape (Fig. 5c(iv)) in ANSYS AQWA, the stress experienced by the floater significantly increases, aligning closely with our experimental findings.

Furthermore, we conducted a cross-comparison of the dynamic performance among the roller, elastomer, and assist modes (Fig. 5d), using the steel roller model as a reference (Figs. 5e(i) and (ii)). The partially constrained modes, such as K1 and M3, outperformed the steel roller mode in both translational and rotational aspects, indicating that increasing inertia can weaken the dynamic performance of the F-TENG shell (Fig. 5e(i)). In F-TENG, modes with complete freedom of movement like the roller or with restrict free movement like springs, will transfer a portion of the energy to the internal moving components under external wave excitation, as metaphorically shown in Fig. 3a(iv). The more energy is transferred, the more comprehensive the internal motion becomes, potentially leading to improved triboelectric charging effects. The introduction of appropriate external assistance can enhance the oscillations of F-TENG, as shown in Figs. 5e(i) and (ii), resulting in increased rotational energy while slightly diminishing translational performance. Under the influence of surface waves, external assisting bodies act as levers in conjunction with the F-TENG main body, thereby driving its motion and generating greater oscillations. We also used ANSYS AQWA to simulate the stress experienced by the fully free-moving roller mode under the same wave excitation (Fig. 5f(i) and Movie S2). By adjusting the density of the rolling ball in the model to increase its mass, we observed a corresponding increase in stress after running the Hydrodynamic Diffraction module. Similarly, after modeling pendulum size diagram (with diameters of 12, 4 cm for the main body and pendulum ball, respectively), we explored the effect of rod length (4, 8 cm) on the swinging state. During simulated resonance waves, the introduction of the rod significantly increased the stress on the surface of the pendulum-shaped float, example the stress increased from the usual value of around 100 to 227.93 mN, as shown in Fig. 5f(i) left. However, an excessively long pendulum may result in a diminished assisting effect.

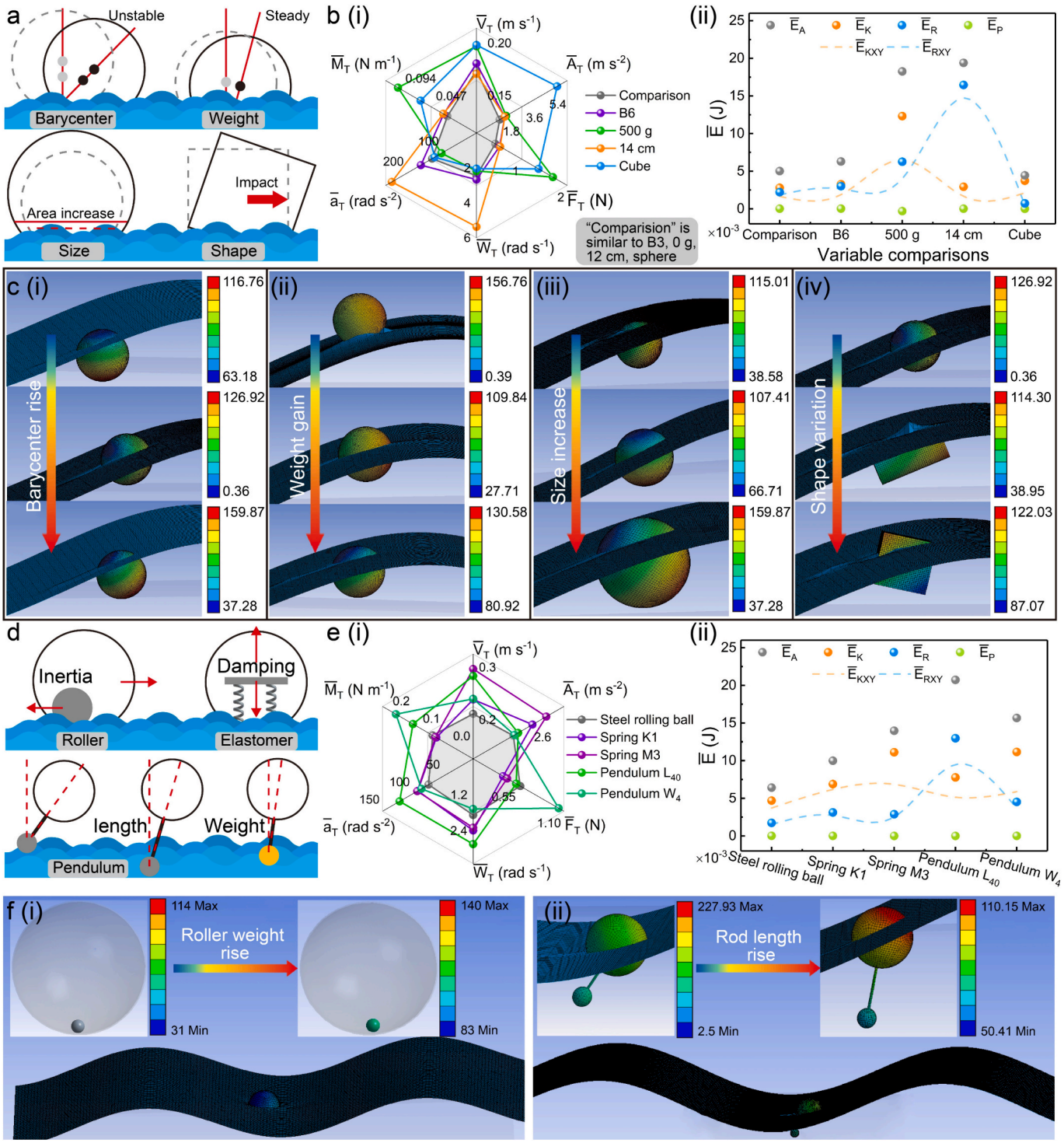

Fig. 5. Comparison and simulation analysis of variations. (a) Comparative analysis charts, (b) (i) dynamic radar charts, (ii) energy curve graphs, and (c) ANSYS AQWA simulation diagrams ((i) barycenter, (ii) weight, (iii) size, (iv) shape) of geometric parameter variations in the floats following lateral comparisons. (d) Comparative analysis charts, (e) (i) dynamic radar charts, (ii) energy curve graphs, and (f) ANSYS AQWA simulation diagrams ((i) completely free roller mode, and its behavior can resemble the semi-free elastomer mode, (ii) pendulum mode one of the external assists) for lateral comparisons among the mode variations.

3.6. *Universal analysis and application perspectives*

The selected parameters and modes, including barycenter, weight, size, shape (e.g. sphere, cylinder, cube, and other [28]), roller (e.g. rolling ball and cylinder [32,39]), elastomer [22,25], and assist (e.g. inner, outer pendulum [33,35], and outer gear [36]), have been distilled from F-TENG articles over the past decade, from 2013 to 2023, as illustrated in Fig. 6a. The number of articles exploring parameters or modes is displayed in each pie chart, with detailed information is shown in Table S3. Among them, except for a few gear-shaped F-TENGs [36], almost all of them will change the barycenter in operation. These variables are widely encompassed in most of these articles, serving as fundamental factors or conventional modes of operation, underscoring their universality within the field of F-TENG.

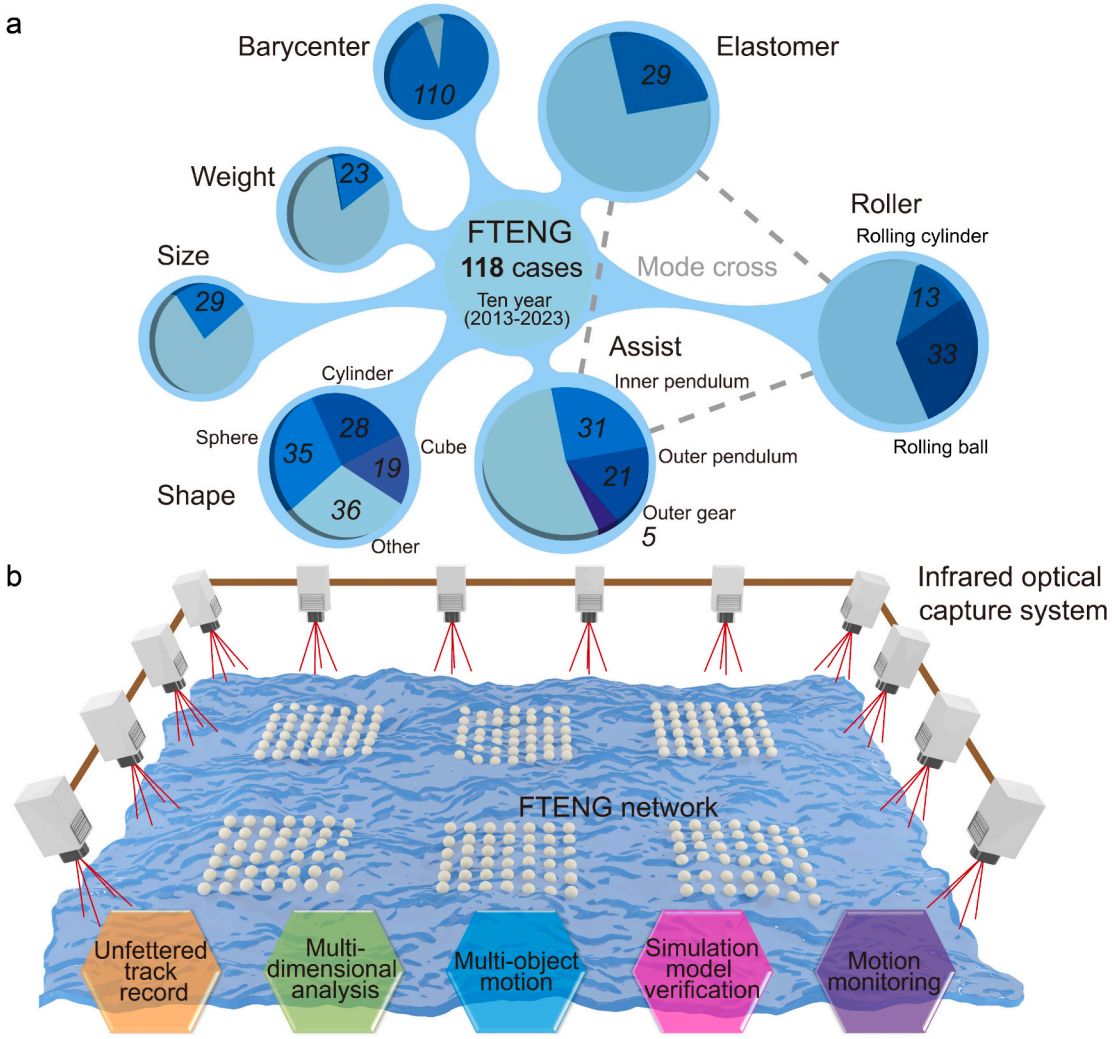

Fig. 6. Universal analysis. (a) Model universality. In this analysis, a total of 118 high quality articles related to F-TENG, published between 2013 and 2023, were selected as the dataset (detailed information as shown in the Table S3). The study focused on calculating the proportion of each parameter/mode within these articles, and the quantity associated with each were displayed in the statistical graph. Due to overlapping content, the combined reviews of the three modes - roller, elastomer, and assist - exceed the total count of 118 articles. (b) Method universality. The IOCS is exceptionally well-suited for trajectory tracking, multidimensional and multi-object dynamic analysis, simulation validation, and motion monitoring of F-TENG unit and networks, which provides a precise set of measurement tools, facilitating the practical testing of F-TENG.

The chosen method of IOCS allows for precise tracking of the six degrees of freedom for individual and multiple rigid bodies within its scope, as depicted in Fig. 6b, which perfectly aligns with F-TENG's trajectory tracking, multi-dimensional analysis, multi-object and networked motion analysis, model simulation validation, and motion monitoring. Its universal applicability in testing scenarios provides a novel means of conducting dynamic research in the field of F-TENG.

4. Conclusions

In this paper, we systematically dissected common parameters and modes within F-TENG to create floats with variations in barycenter, weight, size, shape, roller, elastomer, and assist; and employed an infrared optical capture system to experimentally test the motion of these floats under uniform and resonant waves; then derived universal patterns governing the F-TENG variations by utilizing specific dynamic calculations, statistical theories, and ANSYS AQWA dynamics analysis software; and succinctly presented the findings through dynamic radar charts and energy variation curves finally. These derived patterns through multidimensional dynamic analysis and simulations will enable the effective prediction of optimal F-TENG structures, and advance the standardization and practicality of F-TENG technology. The conclusions drawn are as follows:

1) The appropriate upward barycenter, increase weight, and transition from spherical to square shape will comprehensively enhances the translational dynamics, like $\overline{V}_T$, $\overline{A}_T$, $\overline{F}_T$, $\overline{M}_T$, and $\overline{E}_K$. 2) However, the gradually increased weight and number of facets, downsize, lowering barycenter can significantly diminish their ability to rotate and oscillate, resulting in an obviously decrease at $\overline{W}_T$, $\overline{a}_T$, and $\overline{E}_R$. 3) Reducing the weight in the roller mode, the stiffness coefficient and support weight in the elastomer mode, and adding appropriate assistance, like L_{40} and W_3, can effectively increase the F-TENG's dynamic performance and energy absorption of inner triboelectric block. 4) The internal moving block has greater frequency response than the shell or wave, sometimes even several times larger.

Supplementary data to this article can be found online at https://doi.org/10.1016/j.apenergy.2024.123468.

CRediT authorship contribution statement

Shuxing Xu: Writing – original draft. **Jiabin Zhang:** Formal analysis. **Erming Su:** Formal analysis. **Chengyu Li:** Formal analysis. **Wei**

Tang: Funding acquisition. **Guanlin Liu:** Conceptualization. **Leo N.Y. Cao:** Writing – review & editing, Conceptualization. **Zhong Lin Wang:** Writing – review & editing, Supervision, Funding acquisition.

Declaration of competing interest

The authors declare no competing interests.

Data availability

The data that support the plots within this paper and other findings of this study are available from the corresponding authors upon reasonable request.

Acknowledgements

The research was supported by the National Key R & D Project from Minister of Science and Technology (2021YFA1201601), National Natural Science Foundation of China (Grant No. 52192610), and CAS Youth Interdisciplinary Team.

References

[1] Wang ZL. Catch wave power in floating nets. Nature 2017;542:159–60.
[2] Chu S, Majumdar A. Opportunities and challenges for a sustainable energy future. Nature 2012;488:294–303.
[3] Fan F-R, Tian Z-Q, Lin Wang Z. Flexible triboelectric generator. Nano Energy 2012;1:328–34.
[4] Baytekin HT, Patashinski AZ, Branicki M, Baytekin B, Soh S, Grzybowski BA. The mosaic of surface charge in contact electrification. Science 2011;333:308–12.
[5] Wang ZL. On Maxwell's displacement current for energy and sensors: the origin of nanogenerators. Mater Today 2017;20:74–82.
[6] Wang ZL. On the first principle theory of nanogenerators from Maxwell's equations. Nano Energy 2020;68:104272.
[7] Wang ZL, Wang AC. On the origin of contact-electrification. Mater Today 2019;30:34–51.
[8] Wang ZL, Jiang T, Xu L. Toward the blue energy dream by triboelectric nanogenerator networks. Nano Energy 2017;39:9–23.
[9] Xu W, Zheng H, Liu Y, Zhou X, Zhang C, Song Y, et al. A droplet-based electricity generator with high instantaneous power density. Nature 2020;578:392–6.
[10] Xu Z, Cao LNY, Li C, Luo Y, Su E, Wang W, et al. Digital mapping of surface turbulence status and aerodynamic stall on wings of a flying aircraft. Nat Commun 2023;14:1–10.
[11] Li C, Liu D, Xu C, Wang Z, Shu S, Sun Z, et al. Sensing of joint and spinal bending or stretching via a retractable and wearable badge reel. Nat Commun 2021;12:2950.
[12] Zhang C, Tang W, Han C, Fan F, Wang ZL. Theoretical comparison, equivalent transformation, and conjunction operations of electromagnetic induction generator and triboelectric nanogenerator for harvesting mechanical energy. Adv Mater 2014;26:3580–91.
[13] Zhao H, Xu M, Shu M, An J, Ding W, Liu X, et al. Underwater wireless communication via TENG-generated Maxwell's displacement current. Nat Commun 2022;13:3325.
[14] Maharjan P, Bhatta T, Cho H, Hui X, Park C, Yoon S, et al. A fully functional universal self-chargeable power module for portable/wearable electronics and self-powered IoT applications. Adv Energy Mater 2020;10:2002782.
[15] Luo J, Wang ZL. Recent progress of triboelectric nanogenerators: from fundamental theory to practical applications. EcoMat 2020;2:e12059.
[16] Su E, Li H, Zhang J, Xu Z, Chen B, Cao LNY, et al. Rationally designed anti-glare panel arrays as highway wind energy harvester. Adv Funct Mater 2023;33:2214934.
[17] Liu G, Chen J, Tang Q, Feng L, Yang H, Li J, et al. Wireless electric energy transmission through various isolated solid media based on triboelectric nanogenerator. Adv Energy Mater 2018;8:1703086.
[18] Tian J, Feng H, Yan L, Yu M, Ouyang H, Li H, et al. A self-powered sterilization system with both instant and sustainable anti-bacterial ability. Nano Energy 2017;36:241–9.
[19] Han J, Liu Y, Feng Y, Jiang T, Wang ZL. Achieving a large driving force on triboelectric nanogenerator by wave-driven linkage mechanism for harvesting blue energy toward marine environment monitoring. Adv Energy Mater 2022;13:2203219.
[20] Liu GL, Guo HY, Xu SX, Hu CG, Wang ZL. Oblate spheroidal triboelectric nanogenerator for all-weather blue energy harvesting. Adv Energy Mater 2019;9:1900801.
[21] Feng J, Zhou H, Cao Z, Zhang E, Xu S, Li W, et al. 0.5 m triboelectric nanogenerator for efficient blue energy harvesting of all-sea areas. Adv Sci 2022;9:2204407.
[22] Wen H, Yang P, Liu G, Xu S, Yao H, Li W, et al. Flower-like triboelectric nanogenerator for blue energy harvesting with six degrees of freedom. Nano Energy 2022;93:106796.
[23] Li C, Xu Z, Xu S, Wang T, Zhou S, Sun Z, et al. Miniaturized retractable thin-film sensor for wearable multifunctional respiratory monitoring. Nano Res 2023;16:11846–54.
[24] Wang X, Niu S, Yin Y, Yi F, You Z, Wang ZL. Triboelectric nanogenerator based on fully enclosed rolling spherical structure for harvesting low-frequency water wave energy. Adv Energy Mater 2015;5:1501467.
[25] Xiao TX, Liang X, Jiang T, Xu L, Shao JJ, Nie JH, et al. Spherical triboelectric nanogenerators based on spring-assisted multilayered structure for efficient water wave energy harvesting. Adv Funct Mater 2018;28:1802634.
[26] Bhatta T, Maharjan P, Shrestha K, Lee S, Salauddin M, Rahman MT, et al. A hybrid self-powered arbitrary wave motion sensing system for real-time wireless marine environment monitoring application. Adv Energy Mater 2022;12:2102460.
[27] Xu G, Li C, Chen C, Fu J, Hou T, Zi Y. Dynamics of triboelectric nanogenerators: a review. Int J Mech Syst Dyn 2022;2:311–24.
[28] Xu S, Liu G, Wang J, Wen H, Cao S, Yao H, et al. Interaction between water wave and geometrical structures of floating triboelectric nanogenerators. Adv Energy Mater 2021;12:2103408.
[29] Chen W, Li Z, Cui X, Zhang J, Bai S. Mechanical design and kinematic modeling of a cable-driven arm exoskeleton incorporating inaccurate human limb anthropomorphic parameters. Sensors 2019;19:4461.
[30] Zhang Q, Liang Q, Nandakumar DK, Qu H, Shi Q, Alzakia FI, et al. Shadow enhanced self-charging power system for wave and solar energy harvesting from the ocean. Nat Commun 2021;12:616.
[31] Liang X, Jiang T, Liu G, Feng Y, Zhang C, Wang ZL. Spherical triboelectric nanogenerator integrated with power management module for harvesting multidirectional water wave energy. Energy Environ Sci 2020;13:277–85.
[32] Duan Y, Xu H, Liu S, Chen P, Wang X, Xu L, et al. Scalable rolling-structured triboelectric nanogenerator with high power density for water wave energy harvesting toward marine environmental monitoring. Nano Res 2023;16:11646–52.
[33] Wang H, Xu L, Bai Y, Wang ZL. Pumping up the charge density of a triboelectric nanogenerator by charge-shuttling. Nat Commun 2020;11:4203.
[34] Zhang XM, Yang QX, Ji PY, Wu ZF, Li QY, Yang HK, et al. Modeling of liquid-solid hydrodynamic water wave energy harvesting system based on triboelectric nanogenerator. Nano Energy 2022;99:107362.
[35] Zhang C, He L, Zhou L, Yang O, Yuan W, Wei X, et al. Active resonance triboelectric nanogenerator for harvesting omnidirectional water-wave energy. Joule 2021;5:1613–23.
[36] Lin Z, Zhang B, Zou H, Wu Z, Guo H, Zhang Y, et al. Rationally designed rotation triboelectric nanogenerators with much extended lifetime and durability. Nano Energy 2020;68:104378.
[37] Cao B, Wang P, Rui P, Wei X, Wang Z, Yang Y, et al. Broadband and output-controllable triboelectric nanogenerator enabled by coupling swing-rotation switching mechanism with potential energy storage/release strategy for low-frequency mechanical energy harvesting. Adv Energy Mater 2022;12:2202627.
[38] Jing Z, Zhang J, Wang J, Zhu M, Wang X, Cheng T, et al. 3D fully-enclosed triboelectric nanogenerator with bionic fish-like structure for harvesting hydrokinetic energy. Nano Res 2022;15:5098–104.
[39] Hong H, Yang X, Cui H, Zheng D, Wen H, Huang R, et al. Self-powered seesaw structured spherical buoys based on a hybrid triboelectric–electromagnetic nanogenerator for sea surface wireless positioning. Energy Environ Sci 2022;15:621–32.